Simple X-ray speckle-pattern correlation interferometer

Rachel Eisenhower,[a]* Rainer Gehrke,[a] Gerhard Materlik,[a] Michael Drakopoulos,[b] Alexandre Simionovici[b] and Anatoli Snigirev[b]

[a]HASYLAB am DESY, Notkestrasse 85, 22603 Hamburg, Germany, and [b]European Synchrotron Radiation Facility, BP 220, 38043 Grenoble CEDEX, France. E-mail: rachel@desy.de

Speckle-pattern correlation interferometry (SPCI) is a well established technique in the visible-light regime for observing surface disturbances. It has found application in non-destructive testing of materials, as well as in medicine. A method of performing SPCI in the X-ray regime is presented. Instead of using surface reflection, small-angle scattering is utilized. The simple geometry consists of one coherent X-ray beam passing through two samples. The calculated resultant speckle field shows highly enhanced sensitivity to relative motion of the samples. Motions are simulated and their corresponding correlation patterns are calculated. Initial experimental results are presented.

Keywords: interferometers; small-angle scattering; speckle-pattern correlation interferometry (SPCI); X-ray speckle patterns.

1. Introduction

With increasingly bright sources of synchrotron radiation becoming available, experimental methods that require highly coherent visible light are continually being appropriated for the X-ray regime. The observation of X-ray speckle (Sutton *et al.*, 1991) and its usefulness in dynamic (Brauer *et al.*, 1995; Dierker *et al.*, 1995) and static (Vartanyants *et al.*, 1997; Libbert *et al.*, 1997) cases has been explored. Recent studies have investigated the dependence of small-angle scattering speckle upon the degree of coherence of the incident beam (Abernathy *et al.*, 1998; Tsui *et al.*, 1998). This paper investigates the feasibility, for the X-ray regime, of perhaps the most useful implementation of speckle in the visible regime: speckle-pattern correlation interferometry (SPCI) (Jones & Wykes, 1983).

SPCI is used in the visible regime for a wide variety of applications, including materials deformation analysis and measurement of fluid flows. The principle is as follows. Two speckle wavefields are superimposed. These wavefields are the result of either one wave that is split and scatters from two samples, or from one sample that is illuminated with plane waves from different directions. The resulting superimposed wavefield is sensitive to *relative* phase changes between the component wavefields; hence the overall sensitivity to sample motion is greatly increased compared with a single speckle field. If the motion is such that the relative phase change at a given point of observation is $2n\pi$, where n is an integer, then there is no observed change in the superimposed wavefield. If, however, the relative phase change is $(2n + 1)\pi$, then the post- and pre-motion wavefields are uncorrelated; the
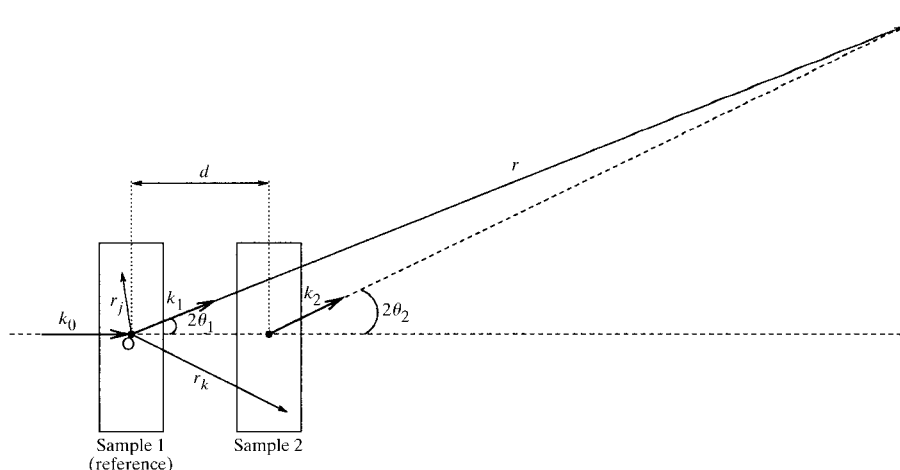

Figure 1
Scattering geometry for double-transmission small-angle scattering.

change in the superimposed wavefield is random. Hence, subtracting the pre- and post-motion speckle patterns produces areas of no intensity where the wavefields were correlated, and speckle where they were not. In the visible region, speckle correlation interferometers usually use a laser beam and a combination of beamsplitters and mirrors to accommodate the geometry required for observing the desired sample motion. This paper explores a simple method of generating two speckle wavefields: the small-angle X-ray scattering of two samples in series.
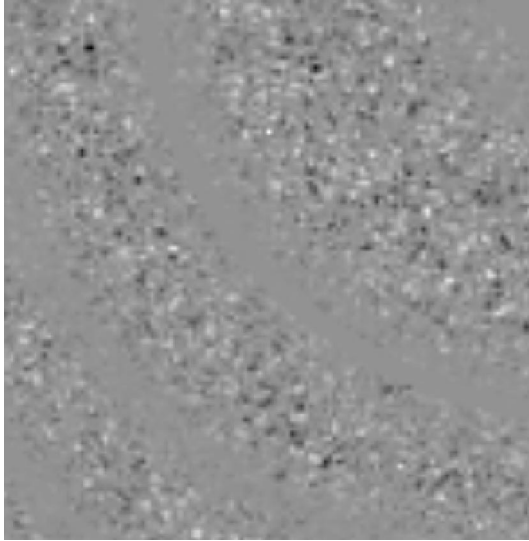

Figure 2
A close-up portion of the difference between simulated speckle patterns, before and after a 100 µm translation of the downstream sample in the longitudinal (parallel to incident beam) direction. The direct-beam location is near the upper right-hand corner, and the image size is 5 mm × 5 mm. The simulated samples–screen distance was 1.5 m.
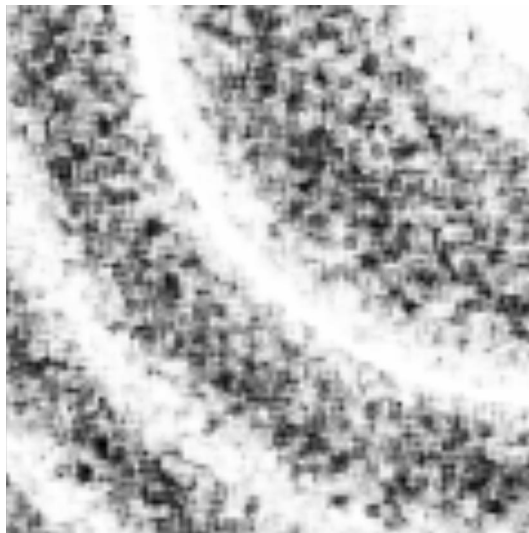

Figure 3
The calculated correlation coefficient between the same two speckle patterns, the difference of which is shown in Fig. 2.

2. Theory and simulations

According to the Green's function formalism, a scattered wavefield $\psi(\mathbf{r})$ can be represented as (Cowley, 1975)

$$\psi(\mathbf{r}) = \psi^o(\mathbf{r}) + \mu \int G(\mathbf{r}, \mathbf{r}') \, \varphi(\mathbf{r}') \, \psi(\mathbf{r}') \, \mathrm{d}\mathbf{r}', \quad (1)$$

where $\psi^o(\mathbf{r})$ is the incident wave, $\varphi(\mathbf{r}')$ is a localized potential and $G(\mathbf{r}, \mathbf{r}')$ is the Green's function. Assuming that each cluster scatters spherically and isotropically leads to a Green function of the form $G(\mathbf{r}, \mathbf{r}') = \exp(ik|\mathbf{r} - \mathbf{r}'|)/4\pi|\mathbf{r} - \mathbf{r}'|$. Assuming an incident plane wave, the first Born approximation is written as $\psi(\mathbf{r}') = \exp(i\mathbf{k}_0.\mathbf{r}')$. Taken together with the approximation $|\mathbf{r} - \mathbf{r}'| \simeq r - \hat{\mathbf{u}}.\mathbf{r}$, where $\hat{\mathbf{u}}$ is a unit vector in the direction of $\mathbf{r}$, the expression for the scattered wavefield becomes

$$\psi(\mathbf{r}) = \psi^o(\mathbf{r}) + \frac{\mu}{4\pi} \frac{\exp(ikr)}{r} \int \varphi(\mathbf{r}') \exp(-i\mathbf{Q}.\mathbf{r}') \, \mathrm{d}\mathbf{r}', \quad (2)$$

where $\mathbf{Q} = \mathbf{k} - \mathbf{k}_0$ is the scattering vector, with magnitude $Q = 4\pi \sin(\theta)/\lambda$, where θ is half the scattering angle.

If the potential consists of a collection of discrete scatterers at positions $\mathbf{r}_j$, then

$$\psi(\mathbf{r}) = \psi^o(\mathbf{r}) + (\mu/4\pi)[\exp(ikr)/r] \\ \times \int \sum_j \varphi_j(\mathbf{r}' - \mathbf{r}_j) \exp(-i\mathbf{Q}.\mathbf{r}') \, \mathrm{d}\mathbf{r}'. \quad (3)$$

Making the substitution $\boldsymbol{\rho} = \mathbf{r}' - \mathbf{r}_j$ leads to the expression

$$\psi(\mathbf{r}) = \psi^o(\mathbf{r}) + (\mu/4\pi)[\exp(ikr)/r] \\ \times \sum_j \left[\int \varphi_j(\boldsymbol{\rho}) \exp(-i\mathbf{Q}.\boldsymbol{\rho}) \, \mathrm{d}\boldsymbol{\rho} \right] \exp(-i\mathbf{Q}.\mathbf{r}_j). \quad (4)$$

The integral term enclosed in square brackets is an overall scattering factor for the cluster that describes the strength and spatial distribution of the cluster scattering. Let this 'cluster scattering factor' be denoted as $f_j(\mathbf{Q})$. Then,
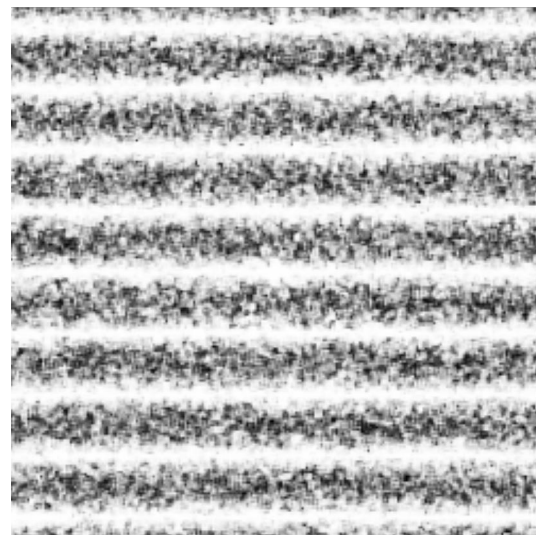

Figure 4
Correlation between simulated speckle patterns, before and after a 0.2 µm vertical translation of the downstream sample. The image size is 5 mm × 5 mm, and the simulated samples–screen distance was 1.5 m.

$$\psi(\mathbf{r}) = \psi^o(\mathbf{r}) + \frac{\mu}{4\pi}\frac{\exp(ikr)}{r}\sum_j f_j(\mathbf{Q})\exp(-i\mathbf{Q}.\mathbf{r}_j). \quad (5)$$

If the clusters are spheres with identical radii a and total electrons per cluster n, the cluster scattering factor can be expressed as (Schwartz & Cohen, 1987)

$$f_j(Q) = n/\exp(aQ/5). \quad (6)$$

If the incident radiation is coherent over the sample dimensions, $\mathbf{Q}.\mathbf{r}_j$ will give the relative phase differences between clusters.

The addition of a second sample, as shown in Fig. 1, yields the scattered field (the term showing the incident beam is no longer shown)

$$\psi(\mathbf{r}) = [\mu\exp(ikr)/4\pi r]\left[\sum_{j=1}^{N}\exp(-i\mathbf{Q}_1.\mathbf{r}_j)f(Q_1)\right.$$
$$\left. + \sum_{k=1}^{N}\exp(-i\mathbf{Q}_2.\mathbf{r}_k)f(Q_2)\right]. \quad (7)$$

The atoms in the second sample are assumed to be the same quantity and type as in the first, but with different positions. Since the scattered field depends on the *relative* positions, it has increased sensitivity to motion of one of the samples.

Fig. 2 shows a portion of the difference in $|\psi(\mathbf{r})|^2$ before and after a 100 µm translation of the downstream sample in the longitudinal (parallel to incident beam) direction. Regions of correlation are visible as solid (unspeckled) bands. The amount of correlation between pre- and post-motion images can be quantified by calculating the correlation coefficient, ρ (Goodman, 1985). ρ is a measurement of the similarity between random variables U and V,

$$\rho = C_{UV}/(\sigma_U\sigma_V), \quad (8)$$

where C_{UV} is the covariance of U and V ($C_{UV} = \overline{UV} - \overline{U}\,\overline{V}$), and σ is the standard deviation. The correlation coefficient varies between -1 and 1. In the figures, white corresponds to $\rho = 1$, or complete correlation. The value of ρ for a given pixel is calculated by selecting a small sub-array of pixels about the pixel of interest, and computing the covariance of the two images for this sub-array of pixels. This covariance is normalized by the product of the standard deviations for each sub-array. This normalization makes the areas of correlation/decorrelation more visible when a large varia-

tion in image intensity is present, as is typically the case in small-angle scattering. Its use is also advantageous for uneven exposure times or intensities between images. Fig. 3 shows ρ corresponding to Fig. 2. White is $\rho = 1$, or correlation. Fig. 4 shows a 0.2 µm translation of the downstream sample in the vertical direction. Without the presence of the upstream reference sample, ρ is almost 1 for the entire image. The direct-beam location is in the middle of the image. The simulations for Figs. 2, 3 and 4 were performed for an 8 keV incident and perfectly coherent beam, a 3 µm $\times$ 3 µm $\times$ 500 µm sample size, a sample–screen distance of 1.5 m (measured from the upstream sample), an initial separation between the samples of 0.5 cm, and a 5 mm $\times$ 5 mm image size.

3. Experiment

The experiment was performed at the undulator beamline ID22 of the European Synchrotron Radiation Facility (ESRF). The beamline is optimized for delivery of coherent hard X-rays. For this experiment the third harmonic of the undulator radiation was used at a gap setting of 17.26 mm, producing 8 keV radiation. A flat highly polished Si mirror and a fixed-exit Si(111) monochromator were used. A sketch of the experiment is shown in Fig. 5. A 20 µm-diameter Pt pinhole was used to collimate the incident beam. A 50 µm guard pinhole was used immediately prior to the first sample for reduction of air scattering. The first sample was mounted on a piezoelectric translator in the hope of achieving better linearity of movement than obtainable with a stepper motor. The piezo itself was mounted on a rotation stage for the purpose of aligning the sample motion with the beam direction. The downstream sample was also moveable by use of horizontal, vertical and longitudinal translation stages.

The samples were Pd-loaded silicone polymer membranes, originally developed by Dr Detlev Fritsch of the GKSS Forschungzentrum in Geestacht, Germany, for catalytic usage. The Pd concentration is at least 15% by weight, with a mean cluster diameter of $\sim$80 Å. See Fritsch & Peinemann (1995) and Tröger et al. (1997) for details of the membrane preparation and characterization. The sample thickness was 0.32 mm and the measured absorp-
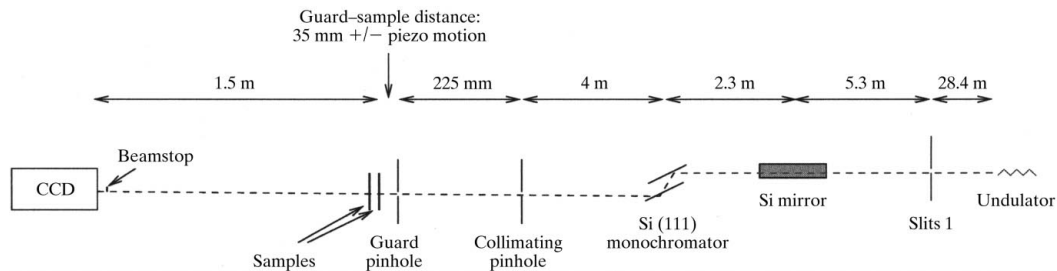
Figure 5
Sketch of the experimental set-up. The typical separation between samples was 5 mm. The downstream sample was the stationary reference sample, and the upstream sample was mounted on a piezo-controlled drive. The pinhole diameters were 20 µm for the collimating and 50 µm for the scatter-guard.

tion coefficient was $\mu = 9.7$ mm^{-1}. The detector used was a CCD camera fitted with a 1:3 magnifying fibre-optic taper to obtain high (approximately 10 µm) spatial resolution. The CCD pixel size was 22.5 µm. When a reference sample was present, the initial separation between reference and object samples was 5 mm. An example of the speckle pattern observed from one of the samples is shown in Fig. 6.
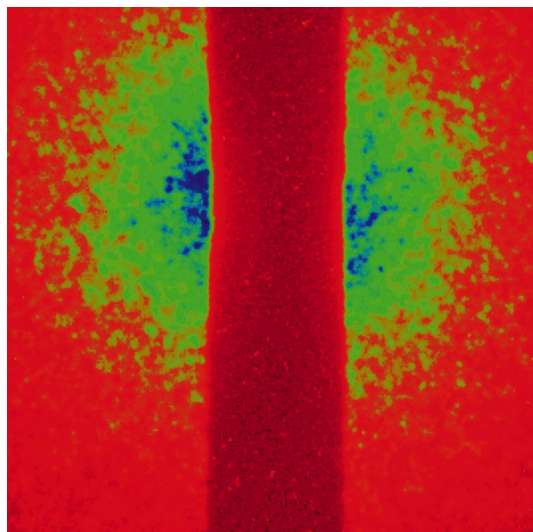

Figure 6
Small-angle scattering from one sample. The vertical band is a 0.5 mm-diameter platinum wire beamstop. The exposure time was 5 min at a ring current of 170 mA.

The thick vertical band is the beamstop, a 0.5 mm-diameter Pt wire. Each individual speckle pattern had an exposure time of 5 min.

Fig. 7 shows the correlation between pre- and post-sample motion for (*a*) without reference sample, 47.6 µm translation, (*b*) with reference sample, 47.6 µm translation, and (*c*) with reference sample, 87.4 µm translation. The image sizes are 3.5 mm × 3.5 mm. Also shown on each correlation figure are horizontal lines. The values of the correlation coefficient along these lines are shown as *xy* plots beneath the corresponding correlation figures. In order to more easily discern information from the *xy* plots, the value at each pixel has been obtained from smoothing (*i.e.* locally averaging) with a 12-pixel-wide smoothing window. When no reference sample is present the correlation coefficient as seen in the *xy* plot of Fig. 7(*a*) is very close to unity at low scattering angle, where there is a lot of signal. As the amount of signal decreases, the correlation coefficient decreases due to noise. When a reference sample is present, as for the plots of Figs. 7(*b*) and 7(*c*), areas of markedly decreased correlation occur, primarily along the horizontal direction. Two such areas are labelled *B* and *C* in the horizontal line-cut of Fig. 7(*b*). These areas of relative decorrelation are proof that the resultant scattered field from two samples in series has enhanced sensitivity to motion of one of the samples, as a result of some degree of coherent addition of reference and object wavefields. Another encouraging qualitative feature is the appearance of finer-spaced areas of decorrelation for a
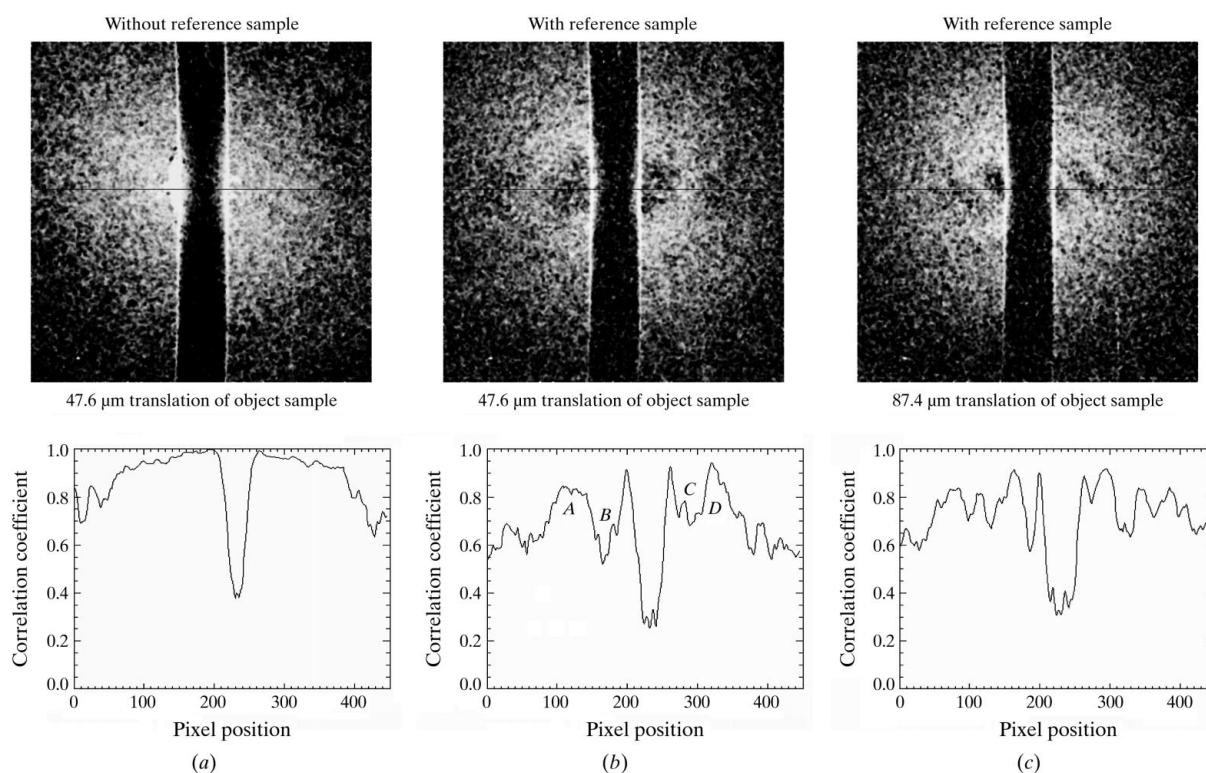

Figure 7
The calculated correlation between before and after motion of the object (upstream) sample. The direction of motion was away from the downstream sample. The image sizes are 3.5 mm × 3.5 mm.

larger sample translation, as can be seen by comparing Fig. 7(c) with Fig. 7(b). This inverse relationship between fringe spacing and translation distance is also seen in the computer simulations.

Although the amount of signal is too small to enable rigorously quantitative fits, the observed features seen in Fig. 7(b) can be simulated reasonably well by a 46 μm parallel, along with submicrometre lateral motions, as shown in Fig. 8. For this simulation the downstream sample was simulated to be the stationary reference sample in order to match the conditions of the experiment. The peaks labelled A and D in the horizontal line-cut of Fig. 7(b) correspond roughly to peaks A and D in the horizontal line-cut of Fig. 8. Note that the experiment bears resemblance to the simulation only within the area bounded by the dotted lines shown in Fig. 8 and that, even within this area, there is insufficient signal for larger scattering angles.

The inclusion of small lateral motions in the simulation for Fig. 8 is motivated by the previous measurement of small lateral errors in motion of the piezo translator. Since the sensitivity to lateral motions for this particular scattering geometry should indeed be greater than the sensitivity to longitudinal motion (compare the 0.2 μm translation of Fig. 4 with the 100 μm translation of Fig. 2), it is not surprising, and indeed an encouraging experimental verification of lateral sensitivity, that the small lateral motions are detected.

4. Conclusions and outlook

These results show that it is possible to perform speckle-pattern correlation interferometry by observing the resultant small-angle scattering from transmission through two samples in series. As was the case for the development of SPCI with visible light, our future efforts will focus on the exact correspondence between observed correlations and sample movement. This we have been able to calculate (see Appendix A) but need higher-quality data with more in-plane sample movements for experimental verification. The use of lighter samples that give more signal for larger Q would facilitate the observation of more fringes, thereby reducing uncertainty of fringe appearance due to absorption and lack of signal.

A careful statistical analysis of the single-sample speckle patterns, as described by Abernathy et al. (1998) and Tsui et al. (1998), should be performed in order to determine the degree of coherence of the incident beam, as well as the speckle statistical properties (i.e. contrast, brightness, size). The same statistical analysis should be performed on the two-sample speckle patterns in order to determine the degree to which the patterns are adding coherently. [As described by Dainty (1985), the statistical properties of a speckle pattern resulting from the coherent addition of two constituent patterns, each of which has the same statistical properties, should be the same as those of one of the constituent speckle patterns.] More work also needs to be performed to understand the reason why correlation fringes appeared only in the horizontal direction. Although the criterion for coherent superposition of wavefields of keeping all scattering pathlength differences within the coherence volume has been satisfied for the longitudinal direction (see Fig. 9), the lack of fringes in the vertical direction suggests that the fields were not adding coher-
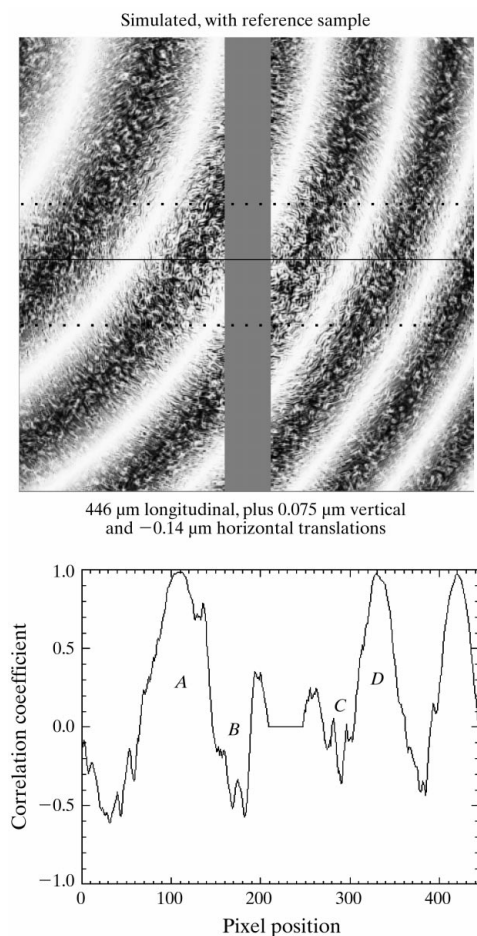

Simulated, with reference sample

446 μm longitudinal, plus 0.075 μm vertical and −0.14 μm horizontal translations

Figure 8
The theoretical correlation between before and after motion of the object sample, with simulated beamstop for reference. The area inside the dotted lines corresponds to the area of Fig. 7(b) in which anticorrelation regions are visible. The image size and resolution are the same as in Fig. 7.
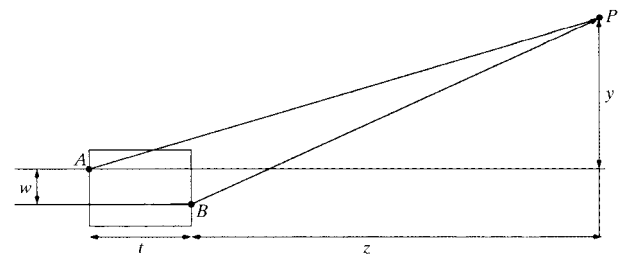

Figure 9
The geometry for calculating the maximum scattering pathlength difference. With the values $y = 1.75$ mm, $t = 5.32$ mm, $z = 1.5$ m and $w = 20$ μm, the maximum pathlength difference is given by $t + BP - AP = 2.7 \times 10^{-8}$ m. The calculated longitudinal coherence length is $\lambda^2/2\Delta\lambda = 5.9 \times 10^{-7}$ m.

ently in the vertical direction. More experimental work needs to be performed to understand the cause.

Although this method does not give a direct high-resolution image, it does give the global sample movement on a submicrometre (for in-plane motion) length scale. Such sensitivity would allow a more accurate determination of stress than measuring, for example, changes in the shape of the small-angle scattering. Such sensitivity could provide a tool to answer questions about directions of movement at the onsets of phase changes, as well as a means of very accurately measuring piezoelectric and ferromagnetic effects. Also possibly valuable is the ability to obtain simultaneously information about the sample's bulk stress and the smaller length-scale variations giving rise to speckle. A present drawback of the method is slowness. In this experiment, as well as in those performed by other researchers obtaining static X-ray speckle photographs, the exposure time is of the order of minutes. SPCI is a method that would benefit from a greater source brightness, as would be available from a free-electron laser (Brinkmann *et al.*, 1997). Also needed is a CCD detector that can provide both high dynamic range and fast readout.

APPENDIX *A*
Fringe location

To obtain a general equation for the description of fringe location, consider a movement of the object sample described by $\mathbf{r}_k \rightarrow \mathbf{r}_k + \mathbf{d}_k$, where $\mathbf{r}_k$ is the scatterer position and $\mathbf{d}_k$ is a displacement vector describing the sample motion. From equation (7) the difference between pre- and post-motion intensity can be written as

$$|\psi_{\text{post}}(\mathbf{r})|^2 - |\psi_{\text{pre}}(\mathbf{r})|^2 = [f(Q_1)f(Q_2)/r^2]$$
$$\times \sum_{j=1}^{N}\sum_{k=1}^{N}\left[2\cos(\mathbf{Q}_1.\mathbf{r}_j - \mathbf{Q}_2.\mathbf{r}_k\right.$$
$$\left. - \mathbf{Q}_2.\mathbf{d}_k) - 2\cos(\mathbf{Q}_1.\mathbf{r}_j - \mathbf{Q}_2.\mathbf{r}_k)\right],$$

which is zero for $\mathbf{Q}_2.\mathbf{d}_k = n\pi$, where n is an integer. Hence, this condition describes the areas of correlation. Note that for rigid-body motion, $\mathbf{d}_k = \mathbf{d}$ is independent of scatterer positions within the sample. For more complicated motions,

the areas of correlation are given, as described by Jones & Wykes (1983), by $\mathbf{Q}_2.\mathbf{d}_{l,\text{max}} = 2n\pi$, as long as the maximum displacement occurs along a boundary of the scattering region. Note that this description for fringe location is quite general and could be extended to other scattering geometries.

References

Abernathy, D. L., Grübel, G., Brauer, S., McNulty, I., Stephenson, G. B., Mochrie, S. G. J., Sandy, A. R., Mulders, N. & Sutton, M. (1998). *J. Synchrotron Rad.* **5**, 37–47.

Brauer, S., Stephenson, G. B., Sutton, M., Brüning, M., Dufresne, E., Mochrie, S. G., Grübel, G., Als-Nielsen, J. & Abernathy, D. L. (1995). *Phys. Rev. Lett.* **74**, 2010–2013.

Brinkmann, R., Materlik, G., Rossback, J., Schneider, J. R. & Wiik, B. H. (1997). *Nucl. Instrum. Methods A*, **393**, 86–92.

Cowley, J. (1975) *Diffraction Physics*, 2nd ed., §1.5. Amsterdam: Elsevier Science Publishers.

Dainty, J. C. (1985). *Laser Speckle and Related Phenomena*, Springer Verlag Topics in Applied Physics, Vol. 9, 2nd ed, p. 21. Berlin: Springer-Verlag.

Dierker, S. B., Pindak, R., Fleming, R. M., Robinson, I. K. & Berman, L. (1995). *Phys. Rev. B*, **75**, 449–452.

Fritsch, D. & Peinemann, K. V. (1995). *Catal. Today*, **25**, 277–283.

Goodman, J. W. (1985). *Statistical Optics*, p. 17. New York: John Wiley & Sons.

Jones, R. & Wykes, C. (1983). *Holographic and Speckle Interferometry*, 2nd ed. Cambridge University Press.

Libbert, J. L., Pindak, R., Dierker, S. B. & Robinson, I. K. (1997). *Phys. Rev. B*, **56**, 6454–6457.

Schwartz, L. & Cohen, J. (1987). *Diffraction from Materials*, 2nd ed. pp. 423–428. Berlin: Springer-Verlag.

Sutton, M., Mochrie, S. G. J., Greytak, T., Nagler, S. E., Berman, L. E., Held, G. A. & Stephenson, G. B. (1991). *Nature (London)*, **352**, 608–610.

Tröger, L., Hünnefeld, H., Nunes, S., Oehring, M. & Fritsch, D. (1997). *J. Phys. Chem. B*, **101**, 1279–1291.

Tsui, O. K. C., Mochrie, S. G. J. & Berman, L. E. (1998). *J. Synchrotron Rad.* **5**, 30–36.

Vartanyants, I. A., Pitney, J. A., Libbert, J. L. & Robinson, I. K. (1997). *Phys. Rev. B*, **55**, 13193–13202.